MRS Communications (2021) 11:233–243

https://doi.org/10.1557/s43579-021-00028-w

MRS Communications

Research Letter

Ultra-low-power neurotransmitter sensor using novel "click" chemistry aptamer-functionalized deep subthreshold Schottky barrier IGZO TFT

Abhijeet Barua, Department of Electrical Engineering and Computer Science, University of Cincinnati, Cincinnati, OH 45221, USA
Ryan J. White, Department of Electrical Engineering and Computer Science, University of Cincinnati, Cincinnati, OH 45221, USA; Department of Chemistry, University of Cincinnati, Cincinnati, OH 45221, USA
Kevin D. Leedy, Air Force Research Laboratory, Sensors Directorate, Wright-Patterson AFB, Dayton, OH 45433, USA
Rashmi Jha, Department of Electrical Engineering and Computer Science, University of Cincinnati, Cincinnati, OH 45221, USA

Address all correspondence to Abhijeet Barua at **baruaat@mail.uc.edu** and Rashmi Jha at **rashmi.jha@uc.edu**

(Received 31 December 2020; accepted 3 March 2021; published online: 17 March 2021)

Abstract

This report implements for the first time an alkyne-azide "click" chemistry to position dopamine-specific aptamer receptors on InGaZnO (IGZO) thin film transistor (TFT) surfaces for sensitive and selective detection of dopamine. It incorporates catalytic attachment of an alkyne-terminated silane to an azide-anchored aptamer that precludes the need of an intermediate molecular cross-linking bond. The TFTs demonstrate high-gain (~ 1000) Schottky action in deep subthreshold regime achieved through high-quality metal–semiconductor contact engineering which enables almost unity voltage operation. The aptamer is specifically synthesized for selectivity towards dopamine and volt-order-calibrated responses with empirical and theoretical detection limits of 1 nM and 100 pM are achieved.

Introduction

Aptamer-based label-free detection of biomolecules is attracting interest lately for their excellent reception with high selectivity and specificity. The 3D structure of aptamers coupled with short strand length when attached to a surface facilitates recognition within the Debye–Hückel limit. Real-time dynamics of chemical messenger molecules in nervous systems, known as neurotransmitters (NTs), are crucial to understand neuronal influences on brain functions, information processing, and other neurochemical processes.[1–6] Dopamine [2-(3,4-dihydroxyphenyl) ethylamine] is an important catecholamine NT that plays a crucial role in the central nervous (CNS), hormonal, renal, and cardiovascular system and helps in the control of cognitive/motor and neuroendocrine functions. Imbalances in dopamine secretion can lead to neurological disorders such as post-traumatic stress disorder, Schizophrenia, Parkinson's, and Alzheimer's disease.[7–9] Such small molecules must be detected with high sensitivity below clinical concentrations, with minimal bio-toxicity levels and high selectivity against interferants. The range of physiological concentration of dopamine within the human blood-brain barrier (CNS) varies between 4.8 ± 1.5 nM in the ventral tegmental area (VTA) and 0.5 ± 0.2 nM in the red nucleus with 10 pM–1 mM ranges in other peripheral components such as adrenal glands, serum, and plasma.[10, 11] Apart from *in vivo* sampling, optical methods, nuclear imaging, and electrochemical detection of NTs, electronic field effect transistors (FETs) offer a platform to transduce the change in charged aptamer morphology on target binding into amplified electrical signals. However, they need to be ultralow power and portable on flexible substrates for seamless integration with micro-probes or wearable devices. These features can be incorporated by the use of amorphous oxide semiconductors, specifically ZnO-based materials *viz.* IGZO, which demonstrate high mobility, low process complexity, low thermal budgets, good flexibility, stability in threshold voltage, and reduced leakage due to the wide bandgap.[12, 13] IGZO is a unipolar, stable three-cation quaternary compound and wide bandgap semiconductor (3.25 to 3.3 eV) that promises lower leakage.[14–16] Indium (In) increases oxygen vacancies in the overall amorphous microstructure which leads to an abundance of unbound metal atoms that leave more electrons free to increase the carrier density. The mobility is enhanced as the *s* orbital is isotropic and larger which leads to better overlap between successive orbitals and, therefore, highly mobile *ns* transport. However, binary oxides of In may be unsafe above critical cytotoxicity levels, because among In, Ga, and Zn, it is the only highly toxic material and, therefore, a ternary combination makes more sense. Ga is known to suppress mobility to semiconductor levels as it bonds O strongly than In or Zn, which creates a stable metal–O–metal structure. Zn has a strong tendency to crystallize along with mobility enhancement and exhibits small effective mass which decreases the effective density of states and tends to suppress the electron concentration to semiconductor levels. Ga, In, and especially Zn may individually be easily etched by wet methods, but this can be tackled by a ternary combination. The amorphous nature of the material enables incorporation of standard deposition methods compatible with CMOS back end of line (BEOL)

processes and removes the need for channel layer doping for contact formation. IGZO is also photosensitive which could allow the integration of future optical modalities along with optoelectronic detection. The flexible nature and easy process flow that include printable and solution-processed methods can soon allow simpler and cost-effective mass manufacture. Whereas high drive current is an important criterion for IGZO TFTs in display driver circuitries and was the fundamental motivation, low-power operation, noise immunity, and high sensitivity become important when it comes to new-found biosensor applications.[17–21] IGZO TFTs have been predominantly explored at near-threshold conditions that require high bias voltages. Interestingly, recent reports have investigated Schottky barrier (SB) source/drain regions wherein the presence of a reverse-biased Schottky diode facilitates low-power deep subthreshold operation due to gate-bias-induced modulation of current injection or extraction through the modulation of a depletion region.[22–24] Despite such advances, these characteristics have not been utilized in the design of FET biosensors. Furthermore, surface chemistry for aptamer immobilization has scarcely evolved to prevent channel/device degradation. In this paper, we report the integration of a direct alkyne-azide chemistry with high-gain Schottky barrier TFTs to achieve sensitive and selective detection of dopamine and propose a biosensor design framework.

Materials and methods

TFT fabrication

TFTs in inverted staggered structure, as shown in Fig. 1(a), were fabricated on a 4″ Si/SiO_2 wafer, including an IGZO post-deposition anneal performed at 200°C to recover device properties, as described elsewhere.[24] No pre- or post-fabrication anneals were performed on the wafer such that virgin characteristics were preserved and the maximum process temperature used was only in atomic layer deposition. The device regions were cleaved and electrically characterized in a Keithley 4200A Semiconductor Characterization System (SCS) with a Cascade Microtech MPS150 Probe Station at room temperature (RT) of 298 K under ambient environment.

Chemicals and reagents

Sylgard® 184 silicone elastomer base and curing agent were purchased from Dow Corning Corporation for casting PDMS wells to hold buffer and target solutions. Silane coupling agent, 90% O-(propargyl)-N-(triethoxysilylpropyl) Carbamate ($C_{13}H_{25}NO_5Si$), which is an olefin functional trialkoxy silane with an alkyne termination group and belongs to the organoethoxysilane chemical family, was purchased from Gelest, Inc. in the liquid form and refrigerated at 4°C. The following were purchased from Sigma-Aldrich (now MilliporeSigma): (i) the catalyst in cross-coupling reactions, 99.999% Copper (I) Bromide (Cu(I)Br) in the powder form and stored at room temperature; (ii) TRIS base (Trizma® base) ((2-amino-2-(hydroxymethyl)-1,3-propanediol) ($NH_2C(CH_2OH)_3$) in the powder form and used as the buffer solution for all major reactions; (iii) ultrapure Tris-EDTA (chemical formula $C_{14}H_{27}N_3O_{11}$) buffer solution with a composition of 10 mM Tris-HCl and 1 mM disodium EDTA at pH 8.0 in the liquid form; (iv) aminoglycoside antibiotic tobramycin, or O-[3-Amino-3-deoxy-α-D-glucopyranosyl-(1→6)]-O-[2,6-diamino-2,3,6-trideoxy-α-D-ribohexopyranosyl-(1→4)]-2-deoxy-D-streptamine target ($C_{18}H_{37}N_5O_9$) without any purification in the powder form and stored at 4°C; (v) synthetic dopamine hydrochloride or 2-(3,4-Dihydroxyphenyl)ethylamine hydrochloride target ($(HO)_2C_6H_3CH_2CH_2NH_2{\cdot}H$) without any purification in the

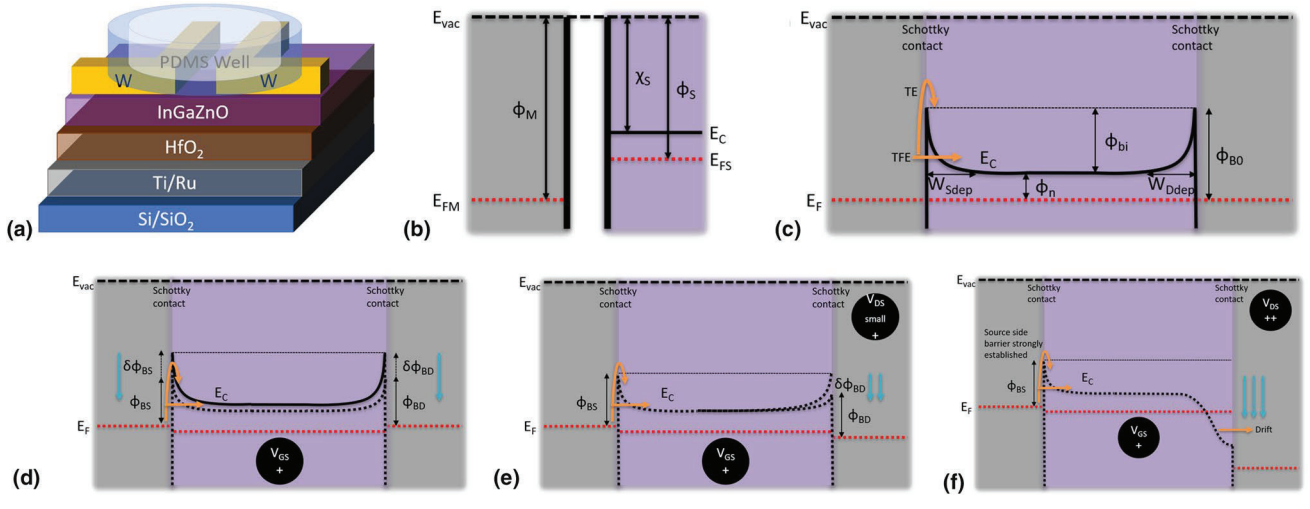

Figure 1. (a) Schematic representation of device setup. (b) Work functions of separate metal and semiconductors. (c) Band bending of the M–S–M junction on combination. (d) Effect of gate bias in lowering initial barrier height for increase in TE and TFE. (e) Effect of small drain bias on drain side forward biased Schottky diode that allows leakage and quasi-linear behavior. (f) Effect of large drain bias that lowers the forward barrier such that carriers are collected through drift transport rather than barrier transport.

powder form and stored at 4°C. Deionized (DI) water was obtained from a Milli-Q Synthesis A10 system. A 57-nucleotide synthetic 1μM dopamine DNA oligonucleotide with a 5′ azide (NHS Ester) modification was obtained from Integrated DNA Technologies after dual-HPLC purification: 5′-azide-GT CTC TGT GTG CGC CAG AGA CAC TGG GGC AGA TAT GGG CCA GCA CAG AAT GAG GCC C-3′.

Stock solutions

167.5 μL of procured TRIS-EDTA buffer solution was centrifuged at 10,000 rpm for 15 s before introduction of dopamine aptamer. Thereafter, calculated amount of 33 nM 5′ azide-modified oligonucleotide was dissolved in TRIS–EDTA buffer without any purification in aliquots such that stock concentration was 0.2 mM (200 μM) of the aptamer and centrifuged again. This stock solution was prepared at pH 8.0 and further divided into aliquots of 10 vials × 2 μL, 3 vials × 20 μL, 1 vial × 10 μL, and 1 vial × < 10 μL, which were stored in a – 20°C freezer and are stable for a long time. The concentration and purity were confirmed through their absorbance spectra on a ThermoScientific BioMate™ 3S UV–Vis spectrophotometer in a 10 mm path length cuvette. 500 mL of 20 mM TRIS buffer was prepared from Trizma (TRIS) powder and DI water in a container and sonicated for 3 min. The pH was adjusted to a final value of 7.0. 250 mL Nalgene rapid-flow filters were used to filter out the buffer solution in a container bottle under vacuum and capped tightly for storage. Thereafter, the ionic buffer was stored in room ambience for further use.

Aptamer immobilization

The devices were cleaned with ethanol, isopropyl alcohol, and DI water, followed by N_2 drying before silanization. Alkyne-terminated IGZO hybrid interfaces were prepared by chemical treatment of the hydroxylated surfaces via undiluted 90% O-(propargyl)-N-(triethoxysilylpropyl) Carbamate drop casted on the devices and laid in a petridish for approximately 16 h overnight reaction. Drops of ethanol were placed around the petridish to prevent drying of the surface. The hydrolyzable group attaches to the hydroxyl-terminated IGZO surface via the covalent Si–O bonds and thus provides a handle for the 5′ azide-terminated non-thiolated DNA to attach. Thereafter, the surface was rinsed again with ethanol and DI water. Cu(I)Br is a coarse amorphous powder and was used as the catalyst for the "click" reaction on IGZO surface. To form a 10 mM strength of aptamer buffer solution, calculated amount of Cu(I)Br crystal was added to 5 mL 20 mM TRIS buffer in a volumetric flask and vortexed for a minute. The 2 μL DNA stock aliquots were centrifuged at 10,000 rpm for 15 s. The reduction of 200 μM aptamer stock to 200 nM concentrations for aptamer immobilization was implemented through a 1000-fold dilution. Entire 2 μL aliquot of 200 μM aptamer stock was mixed with 2 mL of 10 mM Cu(I)Br/TRIS solution as above and vortexed for a minute. This final aptamer solution was then dropcasted on the relevant silanized devices with a cap of DI water present in the petridish so that evaporation is minimal at room ambient temperature. The incubation was varied between 10 min and 18 h and stable data were observed from 10 min incubated devices. Thereafter, 10 min was fixed as the standard incubation time for the rest of the experiments followed by an ethanol/DI water rinse and N_2 drying.

Target preparation

Dopamine target is photo-unstable and, therefore, needs to be prepared just before target conjugation to aptamers for characterization studies. To activate dopamine, it was dissolved in 0.1 M HCl (pH ~ 1.14). 100 mL final volume of 0.1 M HCl solution in DI water was prepared from 12.1 M HCl original solution and vortexed for a minute. To prepare a 1 mM stock concentration of dopamine target (molecular weight 189.64 g/mol), dopamine hydrochloride was dissolved in 20 mL 0.1 M HCl solution prepared above and vortexed again. Three target concentrations of 1 nM, 10 nM, and 100 nM for target detection were then prepared in 20 mM TRIS buffer through serial dilution for electrical tests with rinse dry cycling. Similarly, the tobramycin target was directly prepared in 20 mM (0.1×) of TRIS buffer at concentrations of 1 nM, 10 nM, and 100 nM for real-time electrical cycling tests.[6]

Results

High-gain Schottky behavior

The nature of metal contacts at the source and drain for any TFT dictates the injection or extraction of charge carriers to an extent, along with other factors like control of oxygen vacancies and carrier density. Low resistance ohmic contacts, which are formed when low work function metals are used, can lead to linear behavior, high conductivity, and high mobility in semiconducting carrier concentration oxides ($\leq 10^{16}$ cm^{-3} carrier density), but may come at the cost of switching control loss, high gate leakage and subsequently, and high off current in high carrier concentrations ($\geq 10^{17}$ cm^{-3} carrier density).[24, 25] In such channels, Schottky barriers can be effectively used instead for a tighter conduction modulation due to their non-linear behavior and leakage suppression. This non-ideal interface can be formed under the source/drain contacts by two main approaches. Commonly, the carrier concentration is brought to semiconducting levels at the deposition stage itself by altering the oxygen vacancies through adjustment of the oxygen partial pressure and post-deposition or post-fabrication anneals.[23] The other approach is to use a high work function metal that is abundantly different from the semiconductor work function and, therefore, can form inherent Schottky barriers at the metal–semiconductor–metal (M–S–M) junctions without any adjustment of deposition conditions.

In a M–S combination with an initially high work function difference, the Fermi levels align when they are combined (Fig. 1(b)–(f)). The high work function difference and channel carrier density governs the Schottky barrier height Φ_{B0}, forming a depletion width (W_{Sdep} and W_{Ddep}) which dictates the thermionic emission (TE) over, and thermionic field emission

(TFE) through the barrier. If both source and drain contacts form this interface, then at any point, the transport is dictated by the interplay between the forward- and reverse-biased Schottky barriers. When a positive gate voltage is applied without any drain bias, an accumulation layer of majority carriers is formed that reduces W_{Sdep} and W_{Ddep} and aids TE and TFE. With this fixed gate voltage, and a small bias on the drain terminal, the drain Schottky diode is forward biased and initially governs the leakage and quasi-linear/non-linear transport. This continues until a large drain bias is applied; in which case, the drain carrier collection becomes a drift phenomenon, and source becomes reverse biased. Thus, the saturation current is governed by the reverse saturation transport of this source diode at any given V_{GS}. Hence, there is a gradual transition of the drain barrier limitation to a source limitation with a fixed gate bias and increase in drain bias until the source Schottky barrier concretely dominates the transport.

The Schottky behavior in these long channel devices (W/L = 1625 μm/250 μm) is evident from the linear scale current–voltage trends of the M–S–M layer without any gate bias (Fig. 2(a) and insets). A high resistivity of the channel layer to charge transport was observed. From the reverse-biased Schottky trend, we extracted the effective zero bias barrier height and the ideality factor of the contacts as 0.81 eV and 1.33, respectively. For almost unity operation voltages of these devices, a deep subthreshold region between 10 pA and 1 nA was extracted from the conventional transfer characteristics (Fig. 2(b)). The gate voltage limits were then obtained between $V_{GS\text{-}Lo}$ = 0.9 V and $V_{GS\text{-}Hi}$ = 1.4 V for this deep subthreshold region next to the device off state. Our objective is to operate the biosensor at some point within this regime. To achieve low voltage operation with gate leakage suppression at high gate capacitance and higher accumulation of charge density, HfO_2 high-k gate dielectric was chosen.[26] With a 25-nm-thin HfO_2 insulator layer, the gate leakage was below the pA range. Within this below subthreshold regime, the devices achieved early saturation with the largest drain source transition voltage around $V_{DS\text{-}Tr}$ = 0.26 V at the highest gate voltage of 1.4 V (Fig. 2(c)). Such early transition enables the operation of biosensors in the saturation region around unity voltages so that measured signals do not drift. Almost flat characteristics were obtained in the saturation region which indicated extremely high output resistance. $V_{DS\text{-}Lo}$ was the drain voltage at which drain side barrier lowering allowed the transport to change from a leakage to a quasi-linear behavior (Fig. 2(d)). $V_{DS\text{-}Tr}$ was the drain voltage at which the drain side barrier was lowered to a point where

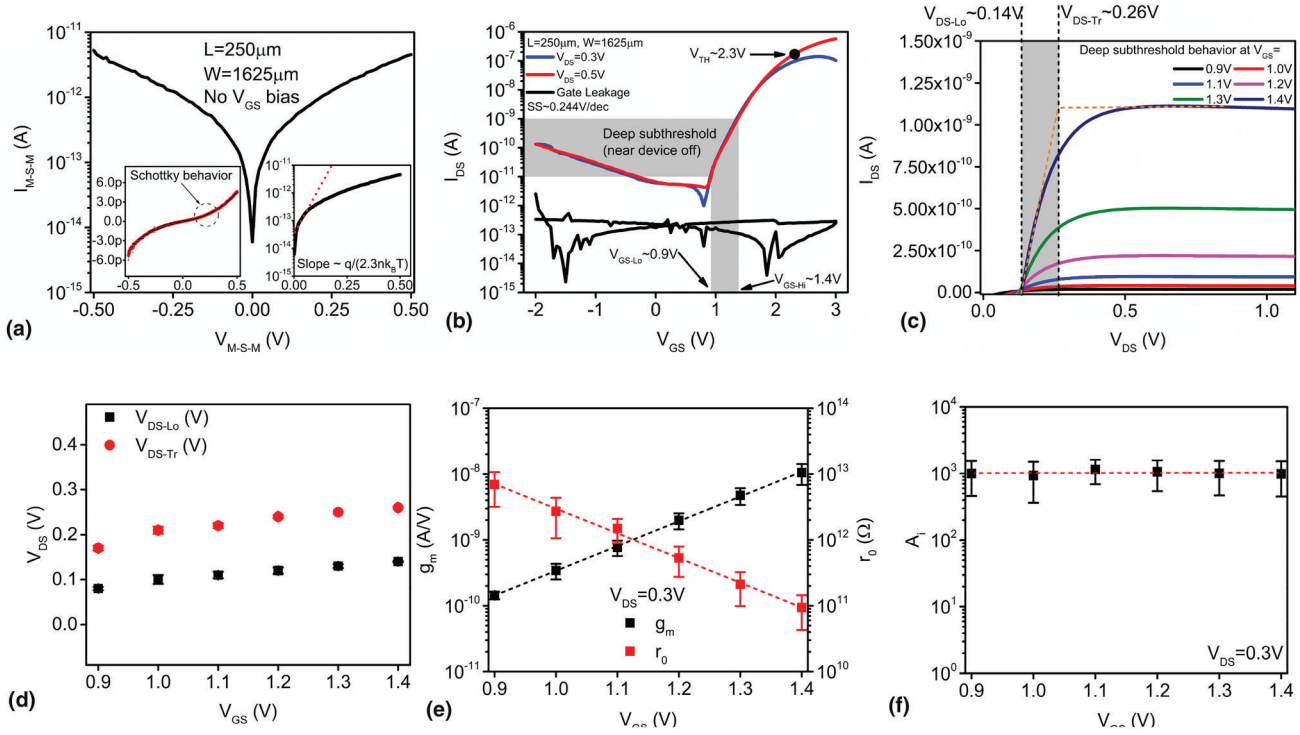

Figure 2. (a) M–S–M current–voltage characteristics that depict the Schottky nature of the barrier and extraction of initial barrier height and contact ideality (insets). (b) Transfer behavior at V_{DS} = 0.3 V and 0.5 V to extract a deep subthreshold regime with low gate leakage. (c) Output behavior within the deep subthreshold regime ($V_{GS\text{-}Lo}$ to $V_{GS\text{-}Hi}$) to obtain the output conductance and resistance for intrinsic gain determination. (d) Variation of the leakage-quasi-linear and quasi-linear-saturation voltages ($V_{DS\text{-}Lo}$ and $V_{DS\text{-}Tr}$) to indicate transition between drain forward biased to source reverse-biased Schottky transport. (e) Variation of the transconductance (g_m) and output conductance (resistance r_0) for extraction of intrinsic gain A_i. (f) Uniform intrinsic gain across the deep subthreshold regime that is approximately two orders of magnitude higher than ohmic TFTs.

the transport changed from a quasi-linear to a saturation one, and therefore, only the reverse-biased source side limited the current. $V_{DS\text{-}Lo}$ and $V_{DS\text{-}Tr}$ remain relatively unchanged between $V_{GS\text{-}Lo}$ and $V_{GS\text{-}Hi}$. Output resistance from output trends and transconductance from transfer curves were obtained within the below subthreshold regime at two drain biases of 0.3 V (Fig. 2(e)) and 0.5 V (not shown). Both parameters had complementary behavior with increments in gate bias. The intrinsic gain for these devices was extracted from the product of the transconductance and the output resistance (Fig. 2(f)). We determined highly stable intrinsic gains (~ 1000) for the device at 0.3 V at such large device dimensions, about an order of magnitude higher than other reported works with much smaller devices. Although the intrinsic gain remained constant through the deep subthreshold regime at V_{DS} = 0.3 V, the highest gain was obtained at gate and drain voltages of 1.3 V and 0.5 V, respectively (not shown). Initial sampling data (not shown) at the noise floor and other voltages (V_{GS} = 1.3 V, V_{DS} = 0.3 V or 0.5 V) within this deep subthreshold region exhibited high stability and similar trends for short time periods of approximately 20 min, which is encouraging for sensor operation, as most temporal resolutions for biomolecule detection lie within this domain. If we consider that our highest transition voltage $V_{DS\text{-}Tr}$ was 0.26 V, then V_{DS} = 0.3 V may be reliably chosen as the drain bias for stable saturation operation, together with V_{GS} = 1.3 V where we observed the highest gain, for the extraction of sensor metrics. In this way, we define the operational regime of these biosensors, contrary to other reports, where such values are chosen arbitrarily. This also blends into the idea that low drain biases ($\ll$ 1 V) should be chosen to stay within the electrochemical window of buffer solutions applied on the IGZO back channel to prevent any local work function change of the source/drain contacts and to sample the target analyte at regular intervals for real-time data.

"Click" chemistry

Nucleic acid aptamers are low molecular weight 3D short chains (20 to 100 nucleotides) of single-stranded DNA or RNA oligonucleotides that can recognize or bind various biomolecules through primary to secondary conformational changes with high affinity (can bind with targets multivalently) and specificity (can recognize single point targets or isomers) due to their predilection to form complementary bonds.[7] Traditionally, the immobilization of aptamers has been mostly a 3-step process with amine-terminated silanization with or without a high-temperature curing procedure, an amine to sulfhydryl/carboxyl group crosslinker or coupling agent that includes ester and maleimide/carbodiimide at opposite ends such as m-maleimidobenzoyl-N-hydroxysulfosuccinimide ester (Sulfo-MBS) or 1-ethyl-3-(3-dimethylaminopropyl)carbodiimide hydrochloride (EDC), and aptamer functionalization to this crosslinker with its own set of chemicals and protocols.[6, 7] This may be harmful to the fragile and sensitive IGZO layer. In fact, devices from our previous ZnO research were damaged due to the lengthened silanization/aptamer immobilization times.[6] We observed surface degradation even under mild solutions, as was used in the buffer or reagent preparation of our previous chemistry, specifically acetonitrile (pH 10.0), crosslinker amine Sulfo-MBS (requires reaction pH 6.5–7.5), NaCl (pH 7.0), $MgCl_2$ (pH 6.0–7.0), and Tris(2-carboxyethyl) phosphine hydrochloride (TCEP) (pH 7.0).

To prevent such an issue, we adopted a method called "click" chemistry, which Sharpless et al. defined as the family of reactions characterized by modular and thermodynamically driven addition of small molecules that enable hetero-atom C–X–C links preferentially over C–C bonds.[27, 28] Essentially, the reaction should meet a set of stringent conditions such as stereospecific nature, high selectivity, singular trajectory to generate a single reaction product, proportionate high yields, generate only easily removeable non-toxic byproducts, and ideally insensitive to water and oxygen that corresponds to use of no or benign solvents. Of many such reaction families, we specifically take the approach of a Cu(I)-catalyzed Azide-Alkyne Cycloaddition (CuAAC) "click" chemistry, in which case, there is high probability of the generation of only the 1,4-isomer reaction product. We chose the reagents such that the dopamine aptamer linked to the rest of the phosphodiester chain through an azide bond, and on the other hand, the silane reagent included an alkyne termination. The main attraction is that this is now reduced to a 2-step process that removes cross-linkers and other harmful chemicals from the equation. Reactions such as $O_2(g) + e^- \rightarrow O_2^-(s)$ and $H_2O(s) + h^+ \rightarrow H_2O^+(s)$ from the surrounding oxygen and adsorbed moisture environment can lead to the formation of predominantly surface hydroxyls (–OH) on unpassivated IGZO back channels.[29] The alkyne-terminated carbamate silane reacts with surface –OH groups to form Si–O covalent bonds that now anchor the silane after a 16 h incubation period (Fig. 3(a)). Ideally, a uniform self-assembled monolayer (SAM) of silane should be created after this condensation reaction.[30] Thereafter, 5′-azide-terminated 57-nt dopamine aptamer was introduced to this Silanized channel for 10 min as mentioned previously. We expect the alkyne and azide groups to conjugate or "click" under the influence of Cu(I) as the catalyst without the need for any other intermediate bond molecules or cross-linkers, which would mean a stable bond, higher surface coverage, and lower steric hindrance.

Figure 3(d)–(l) present the atomic force microscopy (AFM) height and phase topographs and scanning electron microscopy (SEM) micrographs after such physical characterization of the device microstructures at each stage of the 2-step immobilization process to confirm the reaction on the surface. These tests were performed on the pristine device surface, after silanization and after aptamer immobilization on a FEI SCIOS Dual-Beam SEM with T2 imaging detector at 25 pA current, 2 kV energy, magnification of 50,000×, 45° tilt, and 0.1 nA/10 kV current/energy with a collection time of 100 s for energy-dispersive X-ray spectroscopy (EDX) elemental analysis and a Digital Instruments Veeco Dimension 3100 AFM in tapping mode on identical areas. Contrast changes were observed on the surface in SEM images with an increase in granular morphology as

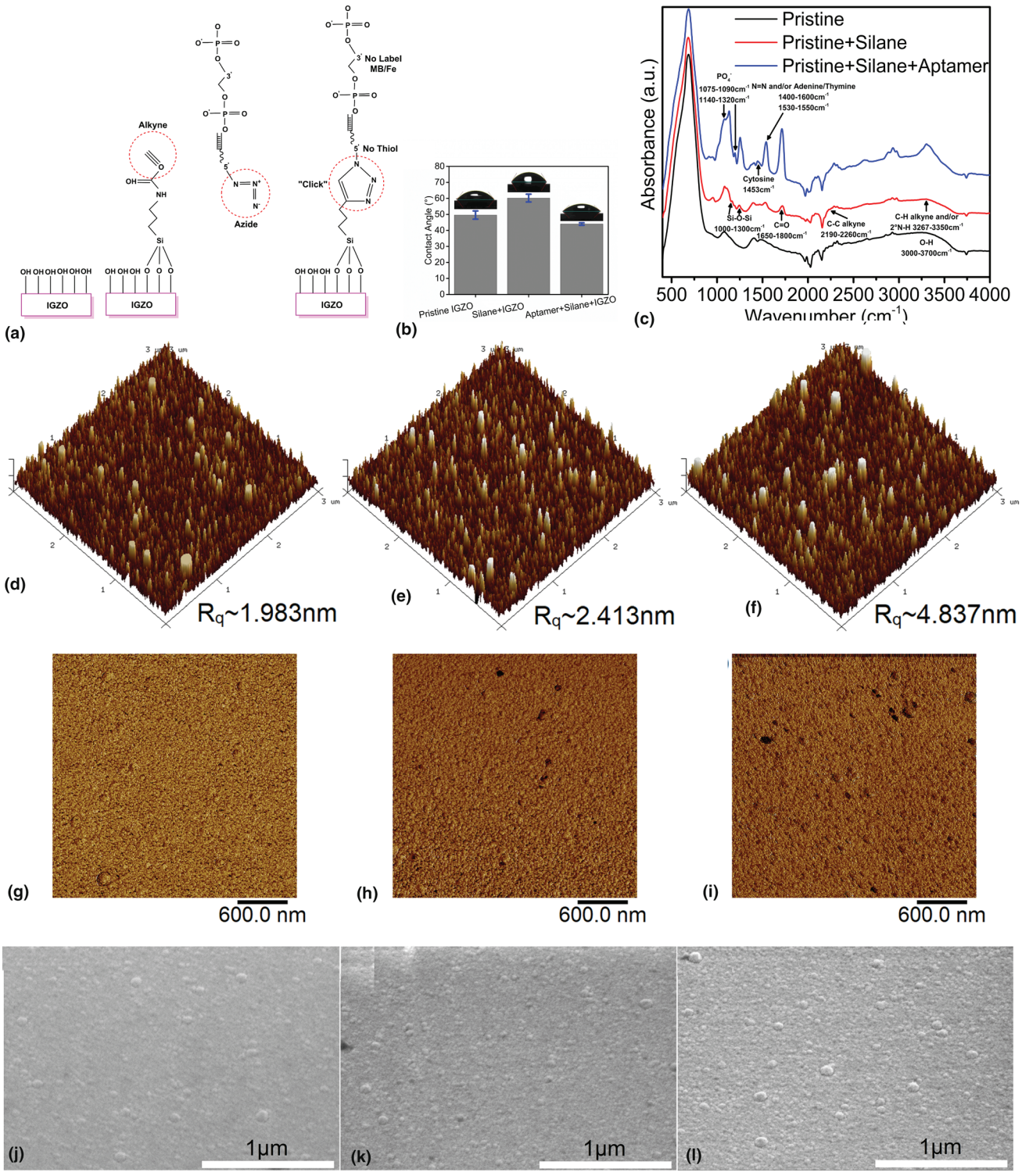

Figure 3. (a) "Click" chemistry-based surface aptamer immobilization sequence. (b) Sessile CA analysis with 1 µL DI water of the pristine device, after undiluted silanization and after alkyne-azide-based aptamer functionalization. (c) ATR-FTIR spectra of the respective surfaces in a wide range between 400 and 4000 cm^{-1}. (d–f) AFM height and surface roughness topographs. (g–i) AFM phase topographs. (j–l) SEM images at a tilt of 45° to observe visual changes.

consecutive steps were performed. EDX spectra and quantitative analysis shows borderline changes in some elements like C, Si, and O, and appearance of new elements like N after silanization and P after aptamer functionalization without any impurity species (Table I). C and Si varied within a $\sigma \sim \pm$ 0.13% and ± 0.84% of weight, respectively, across the samples and exhibited the highest intensity on addition of C and Si rich silane. N, although comparatively minor, appears in the silanized and aptamer-immobilized spectra due to the presence of the 2° N–H bond on the carbamate silane and the alkyne-azide bond, respectively. The phosphodiester deoxyribose in the oligonucleotide allow P to vaguely appear in the final sample. However, at 10 kV, the detector probes through the entire stack till Si, which is orders of magnitude thicker than a few nanometers of surface aptamer chemistry and therefore, surface variation may hide behind bulk elemental signatures and do not correctly represent the reactions happening on top of the channel. Thus, a better fit for such surface analysis would be attenuated total reflectance-Fourier transform infrared (ATR-FTIR) spectroscopy performed on a Nicolet 6700 spectrometer with a diamond crystal ATR in a Smart iTR™ accessory at an incident angle of 42°. Figure 3(c) depicts the ATR-FTIR spectra of pristine IGZO surface and after subsequent functionalization at the silanization step and after aptamer immobilization in a wide range between 400 and 4000 cm^{-1}. A broad peak is evident in the 3000–3700 cm^{-1} range due to the stretching vibration of O–H surface hydroxyls.[31–33] There is a weak appearance of symmetric and asymmetric C–H stretching vibrations in the pristine surface from 2800 to 3000 cm^{-1} which progressively becomes stronger in the silanized and surface-anchored aptamer surfaces due to the presence of C–H groups in the respective constituents. In the silanized sample, a symmetric stretching C–H alkyne peak which may be interspersed with a secondary N–H stretching peak appears in the range 3267–3350 cm^{-1} and a weak asymmetric stretching C≡C alkyne peak appears in a narrow range of 2190–2260 cm^{-1}. The peak observed around 1650–1800 cm^{-1} is an asymmetric C=O stretching vibration. Asymmetric shoulder Si–O–Si and Si–O vibrations are distributed between 1000 and 1300 cm^{-1} and only appear in the silanized and aptamer-functionalized samples. Distinct changes in the spectra can be observed on application of surface-anchored aptamers wherein symmetric and asymmetric PO_4^- peaks from the phosphodiester deoxyribose backbone appear between 1075–1090 cm^{-1} and 1140–1320 cm^{-1}. Another peak between 1400 and 1600 cm^{-1} can be ascribed to –N=N– vibrations flanked by cytosine (1453 cm^{-1}), adenine, and/or thymine (1530–1550 cm^{-1}) from the DNA. FTIR data suggest the confirmation of anchored oligonucleotide after an alkyne-azide conjugation. The AFM topographs indicate an initial pristine IGZO r.m.s. surface roughness (R_q) of ~ 1.983 nm. Thereafter, a progressive roughness increase was observed as more layers of silane and aptamer molecules were added on top. The silane chain length is ~ 0.5 nm, and AFM data at this stage indicated a value of 2.413 nm that could validate the formation of a SAM. With the addition of dopamine aptamer, the surface roughness increased to expected values. The total aptamer length is expected to be ~ 1 to 2 nm and was consistent with AFM data of ~ 4.837 nm after immobilization. AFM phase topographies have also been included to substantiate the addition of the layers as phase is a function of cantilever oscillations and/or derivative of the topography. Therefore, it can be used to distinguish between different species with different mechanical properties to affect the cantilever tip. High-quality IGZO deposition ensures a smoother pristine phase due to finer grains with multiple orientations. This changes to a freckled phase morphology due to the addition of silane SAM and becomes more agglomerated after aptamer adhesion. The physical data together suggest that the surface morphology of IGZO was altered in response to the immobilization protocols that we adopted. Static contact angle (CA) analysis of 1 µL DI water on the different samples was performed through a First Ten Angstroms 1000 B Drop Shape Instrument within 5s to understand surface receptivity to polar Newtonian fluids at the three stages.[34–36] The CA of the pristine surface was 49.6°

Table I. EDX elemental composition spectra obtained from different samples.

Element	Pristine surface		On silanization		Aptamer immobilized surface	
	Weight%	Atomic%	Weight %	Atomic%	Weight %	Atomic%
C K	3.33	10.9	3.52	11.24	3.18	10.59
O K	18.51	45.43	18.09	43.33	17.3	43.18
Zn L	10.67	6.41	9.54	5.59	10.61	6.48
Ga L	4.21	2.37	3.79	2.08	4.48	2.57
Hf M	10.03	2.21	10.06	2.16	10.75	2.41
Si K	11.95	16.7	13.58	18.54	11.65	16.57
Ru L	33.32	12.95	33.63	12.75	31.92	12.61
In L	7.33	2.51	6.35	2.12	7.71	2.68
Ti K	0.65	0.53	0.91	0.73	1.84	1.53
N K	–	–	0.53	1.46	0.42	1.21
P K	–	–	–	–	0.14	0.17
Total	100	100	100	100	100	100

that increased to 60.2° after silanization and decreased to 43.9° after attachment of aptamer (Fig. 3(c)). As per Young's surface energy analysis, CA is inversely related to the surface energy, and the increase in CA on silanization signifies a lower surface energy which in turn establishes the existence of low energy C, H species, and Si molecules that approach hydrophobicity on the surface. Anchored aptamers caused a drop in the CA below even pristine IGZO values due to the tethered negatively charged phosphodiester DNA backbone that increases surface energy and hence adhesion due to higher affinity towards polar DI water molecules.

Sensitivity and selectivity

As depicted in Fig. 1(a), the PDMS wells worked to define the area of the TFT surface exposed to non-physiological buffer, target analyte solutions, and prevent any crosstalk. Devices were physically isolated from each other by sizeable inter-TFT distances (> 5 mm) between them. Additionally, the low gate leakage current negated any contribution to the target signals from the vertical transport component between the gate and the active channel. Some devices with no surface functionalization (non-silanized, non-aptamer immobilized) were exposed to polar solvents such as methanol and DI water (18.2 MΩ) through a 2 μL micropipette to understand the response of IGZO channels to such solvents and how this analysis may be used to distinguish solvent adhesion signals from target-aptamer conjugation signals.[37] On bottom-gated setups, we observed a negative shift in the threshold voltage with hump behavior for both the solvents with a deterioration of the subthreshold slope as shown in Fig. 4(a). The negative threshold voltage shifts without any accompanying appreciable I_{DS} increase points to the accumulation of extra majority carriers near the surface due to the adsorption of polar molecules. In the case of methanol, these polar molecules are volatile, and therefore, the surface accumulation is dependent on the number of molecules present on the surface as the solution evaporates. DI water molecules, due to its longer evaporation time, may be chemisorbed on the channel surface and cause an in-diffusion of H_2O molecules that may require a special heat step or dry step to diffuse out the molecules completely and return the device to its original behavior. The hump behavior can be explained by the sudden increase in surface interface states (different from semiconductor-dielectric interface traps) on solvent introduction, that trapped and released some majority carriers. In all the cases, the devices almost recovered their pristine behavior after a rinse and N_2 drying, albeit with a marginal increase in off current due to the presence of a parallel back channel conduction path from incomplete out-diffusion of

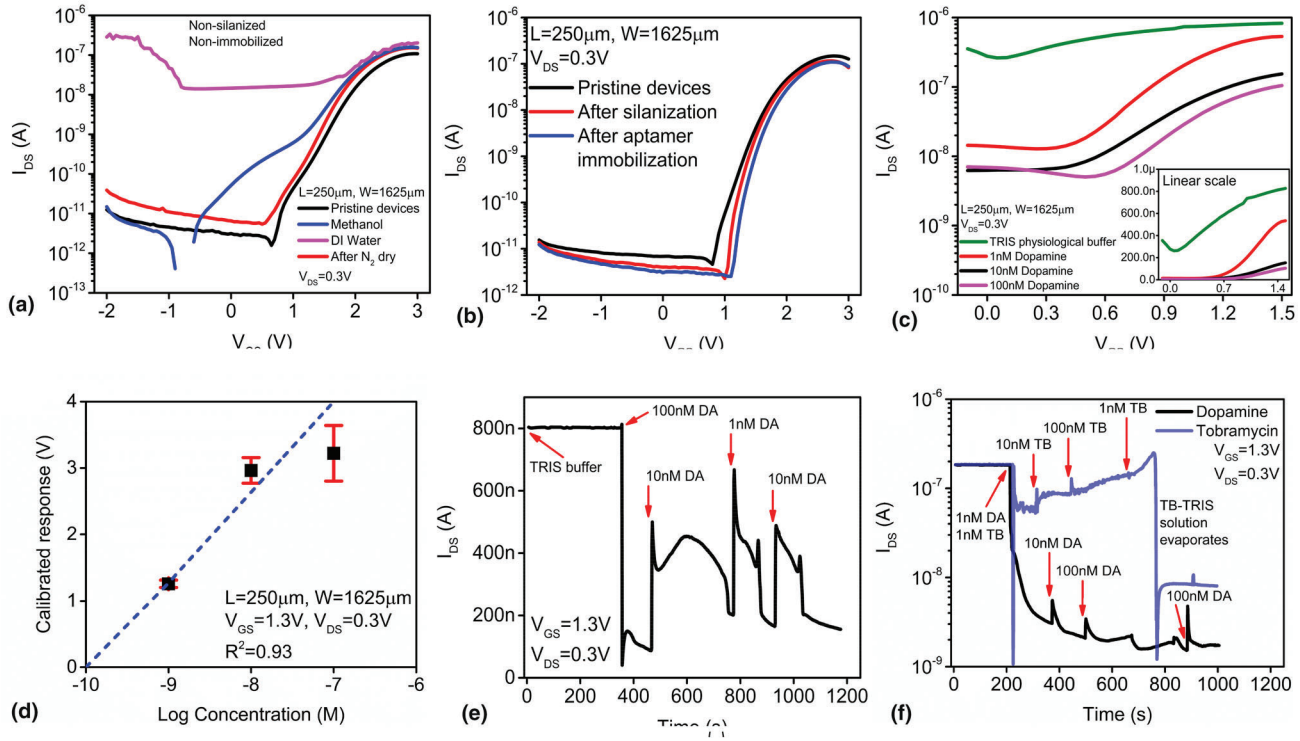

Figure 4. (a) Short-term reversible effect of polar solvents on non-silanized, non-aptamer-functionalized devices. (b) Effect of surface chemistry steps on transfer behavior. (c) Dopamine target-concentration-dependent changes in transconductance against TRIS physiological buffer baseline signals. (d) Calibrated response curve against device transconductance to quantify sensitivity of dopamine detection in the order of volts. (e) Real-time dopamine target-concentration-dependent changes in device transconductance. (f) Real-time selectivity of dopamine detection against tobramycin at different concentrations.

solvent molecules. Therefore, DI water-based buffer solutions may cause a short-term reversible modification of the channel surface, even though they cannot be completely ruled out presently.

Similar transfer curves were again obtained in the standard dry state from another set of silanized and aptamer-functionalized devices as shown in Fig. 4(b) against pristine characteristics to understand the effect of the addition of each of these chemistries. Three sweeps were averaged for each curve and a positive shift in the threshold voltage along with a corresponding incremental decrease in drain current was observed at each of those steps. Within the deep subthreshold regime (10^{-11} to 10^{-9} A), there was slight improvement of the subthreshold slope along with a slight decrease in the off current. Essentially, on silanization, the three alkoxy groups are hydrolyzed in an ethanol environment and then condense to bind through covalent bonds to the IGZO hydroxyl groups. This prevents the $H_2O(s) + h^+ \rightarrow H_2O^+(s)$ conversion and leads to fewer surface accumulation charges that provide an alternate transport path. Thus, a higher electric field is required to establish conduction that leads to a higher threshold voltage with marginal decrease in current. On aptamer functionalization, the aptamer is anchored to the silane through the benzene 1,4 isomer. This introduces the negatively charged phosphor-diester backbones of the DNA aptamer to the channel surface, although with a primary conformational motif. By virtue of the presence of such negative charges in the surrounding environment, there is a top-gating effect which electrostatically repels the surface accumulation charges and leads to the incremental positive threshold voltage shift, although on/off conductance ratio are minimally affected.

Dopamine-specific aptamers were covalently attached to the channel surfaces for electronic detection of synthetic dopamine. The tests were performed in the below subthreshold regime to evaluate the amplification of signals due to target-aptamer conjugation. The devices were tested with only TRIS buffer initially to get the baseline signals. The gate sweep modulated the current along with the salt ions in the buffer that increased the transconductance one order of magnitude higher than common solvents as can be compared between Fig. 4(a) and (c) along with an increase in the off current as well. On the introduction of target analytes to aptamer-tethered surfaces, the primary conformational arrangement of the oligonucleotides is reorganized to a secondary arrangement. From Fig. 4(c), the signal evolution suggests a backbone that approaches the semiconductor spatially in incremental proximity with an increase in dopamine ligand-specific reception such that the conductance is a function of the target concentration. Although dopamine contains a positive charge on its amine group and increased concentration should lead to higher amplification of electronic response due to increased surface accumulation of carriers, our data suggest that this proximal effect is overwhelmed by the multitude of DNA phosphodiester negative charges and causes a drop in drain current. With each increase in target concentration, more surface accumulation charges are electrostatically repelled due to the above action. We observed a change in major parameters of the device on dopamine reception viz. transconductance, on current, and threshold voltage. With these parameters, a mean calibrated response could be extracted from the individual average responses against baseline values (I_{TRIS}–I_{target}) and the corresponding mean transconductance g_m of the device in the deep subthreshold regime for which we designed these sensors (V_{GS} = 1.3 V, V_{DS} = 0.3 V) where g_m takes into account the effect of capacitive gate bias coupling, charge transport (mobility), and channel geometry (W/L) as follows:

$$\text{Calibrated response (V)} = \frac{\{\Delta I_{DS\,(\text{TRIS buffer})} - \Delta I_{DS\,(\text{target concetration})}\}|_{V_{GS}=1.3\text{ V},\,V_{DS}=0.3\text{ V}}}{g_m|_{V_{GS}=1.3\text{ V},\,V_{DS}=0.3\text{ V}}}$$

The mean calibrated signals from three devices provided us with the sensitivity plot Fig. 4(d). Calibrated signals in the order of a few volts were determined compared to traditionally observed mV range of sensitivities, due to the deep subthreshold high-gain design of these sensors. Dopamine was successfully detected from 100 nM linearly down to 1 nM concentrations against TRIS ionic buffer as depicted, and a theoretical limit of detection of 100 pM could be hypothesized from the sensitivity plot. This range of detection is sufficient for the detection of dopaminergic activity within the CNS. However, further optimization of the "click" protocols is required to push these sensors to the fM limits of detection which are observed beyond the brain-blood barrier in the peripheral nervous system,[8] and are under investigation currently.

Real-time data were obtained from functionalized devices with sequential alteration of target concentration to determine response time and reproducibility (Fig. 4(e)). The test was initiated with a TRIS baseline and target solutions were spiked into the wells at intervals. A drop in current response was noticed at 100 nM with eventual average increase in signals with 10 nM and 1 nM. The response time was in the order of seconds; however, it took longer for solutions to equilibrate on the surface and hence the non-saturated response. Successive 10 nM target addition returned the average conductance levels to previous states. The drops at the end of each concentration conductance behavior can be attributed to the crystallization/evaporation of the solution from the well given the fact that a small volume (2 µL) was used for each injection. On another set of identical devices, we obtained real-time data of dopamine (DA) against tobramycin (TB) to evaluate the selectivity of our sensor mechanism (Fig. 4(f)). Again, although the TRIS baseline magnitudes are similar for both the targets, their oligonucleotide-target conjugation signals are almost complementary in nature. Ideally, no non-specific conjugation should occur on device surface; however, unpassivated voids, surface radicals, and physisorption of some molecules could lead to certain steric hindrances such that the slope of such

behavior is non-zero.[38] The change in signals due to similar concentrations of TB is incremental and different than similar changes due to DA, although the percentage change for DA is much higher than for TB. This suggests that our surface chemistry could be specifically used for DA detection against non-specific adsorption of TB.

Discussion and outlook

We described a TFT biomolecule detection mechanism through a unique "click" reaction instead of the traditionally used 3-stage procedure. A facile 2-step surface functionalization immobilizes the dopamine-specific aptamers to the IGZO channel and provides a handle for the reception of target analytes to cause a characteristic change in device behavior. Such a system bestows several merits to the concept of sensitive detection such as the use of high intrinsic gain (~ 1000) devices at almost unity operation voltages, which leads to calibrated responses which are an order of magnitude higher than mV that are conventionally observed and limits the exposure of inorganic channel surfaces to undesirable reagents during the immobilization process which may be detrimental to device performance. The motivation to choose the deep subthreshold regime resonated with this theme to marry maximum sensitivity of target detection to low operation voltages for weak-signal or battery-less operation on a portable platform. The work demonstrates new possibilities to simply tether receptors through a non-toxic, single isomer alkyne-azide product on channel surfaces with high selectivity against other targets as shown against tobramycin. Such a paradigm may play new roles in applications like real-time neurotransmitter monitors, brain function under different circumstances, point-of-care pain detection, and diagnosis of neurological disorders. Specifically, the ability to design aptamer and silane chemistry with a simple conjugation allows for the mix and match approach to tune the detection metrics of the system. Future work will be directed towards functionalization protocol optimization with improvements in device design for even higher signal amplification to obtain lower limits of detection with high sensitivity on flexible platforms to bring it one step closer to mass integration. Additionally, to establish these devices as detection standards, there are opportunities for optimization of selectivity against similar molecules, device passivation, expanded physical characterization, benchmarks against electrochemical tests, and modeling of such reception kinetics.

Acknowledgments

This work was supported by National Science Foundation (NSF) (Grant numbers CNS-1556301, SHF-1718428, and ECCS-1926465). A.B. would like to thank Hope Kumalki, Vamshi Kiran Gogi, Dr. Necati Kaval, Dr. Yao Wu, Dr. Melodie A. Fickenscher, and the ERC Cleanroom and staff at the University of Cincinnati for their help.

Data availability

All data are contained in the primary text.

Declarations

Conflict of interest

The authors declare that they have no conflict of interest.

References

1. S.J. Park, H.S. Song, O.S. Kwon, J.H. Chung, S.H. Lee, J.H. An, S.R. Ahn, J.E. Lee, H. Yoon, T.H. Park, J. Jang, Human dopamine receptor nanovesicles for gate-potential modulators in high-performance field-effect transistor biosensors. *Sci. Rep.* **4**, 4342 (2014)
2. T. Sakata, Biologically coupled gate field-effect transistors meet in vitro diagnostics. *ACS Omega* **4**, 11852 (2019)
3. P.-C. Chen, Y.-W. Chen, I. Sarangadharan, C.-P. Hsu, C.-C. Chen, S.-C. Shiesh, G.-B. Lee, Y.-L. Wang, Editors' choice—field-effect transistor-based biosensors and a portable device for personal healthcare. *ECS J. Solid State Sci. Technol.* **6**, Q71 (2017)
4. I. Sarangadharan, A. Regmi, Y.-W. Chen, C.-P. Hsu, P. Chen, W.-H. Chang, G.-Y. Lee, J.-I. Chyi, S.-C. Shiesh, G.-B. Lee, Y.-L. Wang, High sensitivity cardiac troponin I detection in physiological environment using AlGaN/GaN high electron mobility transistor (HEMT) biosensors. *Biosens. Bioelectron.* **100**, 282 (2018).
5. N. Aliakbarinodehi, P. Jolly, N. Bhalla, A. Miodek, G. De Micheli, P. Estrela, S. Carrara, Aptamer-based field-effect biosensor for Tenofovir detection. *Sci. Rep.* **7**, 44409 (2017)
6. A. Barua, T. H. Nguyen, Y. Wu, V. M. Jain, R. J. White, and R. Jha: in *NAECON 2018—IEEE Natl. Aerosp. Electron. Conf.* (IEEE, 2018), pp. 331–338.
7. N. Nakatsuka, K. A. Yang, J. M. Abendroth, K. M. Cheung, X. Xu, H. Yang, C. Zhao, B. Zhu, Y. S. Rim, Y. Yang, P. S. Weiss, M. N. Stojanović, and A. M. Andrews: Aptamer-field-effect transistors overcome Debye length limitations for small-molecule sensing. *Science* **362**, 319 (2018).
8. J.D. Berke, What does dopamine mean?*Nat. Neurosci.* **21**, 787 (2018)
9. H. Tang, P. Lin, H.L.W. Chan, F. Yan, Highly sensitive dopamine biosensors based on organic electrochemical transistors. *Biosens. Bioelectron.* **26**, 4559 (2011)
10. T.R. Slaney, O.S. Mabrouk, K.A. Porter-Stransky, B.J. Aragona, R.T. Kennedy, Chemical gradients within brain extracellular space measured using low flow push-pull perfusion sampling in vivo. *ACS Chem. Neurosci.* **4**, 321 (2013)
11. S.M. Matt, P.J. Gaskill, Where is dopamine and how do immune cells see it?: Dopamine-mediated immune cell function in health and disease. *J. Neuroimmune Pharmacol.* **15**, 114 (2020)
12. A. Suresh, J.F. Muth, Bias stress stability of indium gallium zinc oxide channel based transparent thin film transistors. *Appl. Phys. Lett.* **92**, 033502 (2008)
13. J.-S. Park, J.K. Jeong, Y.-G. Mo, H.D. Kim, S.-I. Kim, Improvements in the device characteristics of amorphous indium gallium zinc oxide thin-film transistors by Ar plasma treatment. *Appl. Phys. Lett.* **90**, 262106 (2007)
14. R.L. Hoffman, B.J. Norris, J.F. Wager, ZnO-based transparent thin-film transistors. *Appl. Phys. Lett.* **82**, 733 (2003)
15. J.F. Wager, B. Yeh, R.L. Hoffman, D.A. Keszler, An amorphous oxide semiconductor thin-film transistor route to oxide electronics. *Curr. Opin. Solid State Mater. Sci.* **18**, 53 (2014)
16. K. Nomura, H. Ohta, A. Takagi, T. Kamiya, M. Hirano, H. Hosono, Room-temperature fabrication of transparent flexible thin-film transistors using amorphous oxide semiconductors. *Nature* **432**, 488 (2004)
17. Y.-C. Shen, C.-H. Yang, S.-W. Chen, S.-H. Wu, T.-L. Yang, J.-J. Huang, IGZO thin film transistor biosensors functionalized with ZnO nanorods and antibodies. *Biosens. Bioelectron.* **54**, 306 (2014)
18. T.-H. Yang, T.-Y. Chen, N.-T. Wu, Y.-T. Chen, J.-J. Huang, IGZO-TFT Biosensors for Epstein-Barr virus protein detection. *IEEE Trans. Electron Devices* **64**, 1294 (2017)

19. Y.-W. Wang, T.-Y. Chen, T.-H. Yang, C.-C. Chang, T.-L. Yang, Y.-H. Lo, J.-J. Huang, Thin-film transistor-based biosensors for determining stoichiometry of biochemical reactions. *PLoS ONE* **11**, e0169094 (2016)
20. J.T. Smith, S.S. Shah, M. Goryll, J.R. Stowell, D.R. Allee, Flexible ISFET biosensor using IGZO metal oxide TFTs and an ITO sensing layer. *IEEE Sens. J.* **14**, 937 (2014)
21. Y.S. Rim, S.-H. Bae, H. Chen, J.L. Yang, J. Kim, A.M. Andrews, P.S. Weiss, Y. Yang, H.-R. Tseng, Printable ultrathin metal oxide semiconductor-based conformal biosensors. *ACS Nano* **9**, 12174 (2015)
22. J. Zhang, J. Wilson, G. Auton, Y. Wang, M. Xu, Q. Xin, A. Song, Extremely high-gain source-gated transistors. *Proc. Natl. Acad. Sci.* **116**, 4843 (2019)
23. S. Lee, A. Nathan, Subthreshold Schottky-barrier thin-film transistors with ultralow power and high intrinsic gain. *Science* **354**, 302 (2016).
24. A. Barua, K.D. Leedy, R. Jha, Deep-subthreshold Schottky barrier IGZO TFT for ultra low-power applications. *Solid State Electron. Lett.* **2**, 59 (2020)
25. T. T. Trinh, K. Jang, V. A. Dao, J. Yi, Effect of high conductivity amorphous InGaZnO active layer on the field effect mobility improvement of thin film transistors. *J. Appl. Phys.* **116**(21) (2014).
26. X. Ding, J. Zhang, W. Shi, H. Ding, H. Zhang, J. Li, X. Jiang, Z. Zhang, C. Fu, Effect of gate insulator thickness on device performance of InGaZnO thin-film transistors. *Mater. Sci. Semicond. Process.* **29**, 326 (2015)
27. H.C. Kolb, M.G. Finn, K.B. Sharpless, Click chemistry: diverse chemical function from a few good reactions. *Angew. Chem. Int. Ed.* **40**, 2004 (2001)
28. V. Castro, H. Rodríguez, F. Albericio, CuAAC: an efficient click chemistry reaction on solid phase. *ACS Comb. Sci.* **18**, 1 (2016)
29. J. Li, F. Zhou, H.-P. Lin, W.-Q. Zhu, J.-H. Zhang, X.-Y. Jiang, Z.-L. Zhang, Effect of reactive sputtered SiOx passivation layer on the stability of InGaZnO thin film transistors. *Vacuum* **86**, 1840 (2012)
30. X. Du, Y. Li, J.R. Motley, W.F. Stickle, G.S. Herman, Glucose sensing using functionalized amorphous In–Ga–Zn–O field-effect transistors. *ACS Appl. Mater. Interfaces* **8**, 7631 (2016)
31. J.-C. Lin, B.-R. Huang, Y.-K. Yang, IGZO nanoparticle-modified silicon nanowires as extended-gate field-effect transistor pH sensors. *Sens. Actuators B Chem.* **184**, 27 (2013)
32. A. Qureshi, Y. Gurbuz, J.H. Niazi, Label-free capacitance based aptasensor platform for the detection of HER2/ErbB2 cancer biomarker in serum. *Sens.s Actuators B Chem.* **220**, 1145 (2015)
33. M.K. Patel, P.R. Solanki, S. Khandelwal, V.V. Agrawal, S.G. Ansari, B.D. Malhotra, Self-assembled monolayer based electrochemical nucleic acid sensor for Vibrio cholerate detection. *J. Phys. Conf. Ser.* **358**, 012009 (2012)
34. H. Kim, J.-Y. Kwon, Enzyme immobilization on metal oxide semiconductors exploiting amine functionalized layer. *RSC Adv.* **7**, 19656 (2017)
35. P. Xiao, L. Lan, T. Dong, Z. Lin, W. Shi, R. Yao, X. Zhu, J. Peng, InGaZnO thin-film transistors with back channel modification by organic self-assembled monolayers. *Appl. Phys. Lett.* **104**, 051607 (2014)
36. C.G. Allen, D.J. Baker, T.M. Brenner, C.C. Weigand, J.M. Albin, K.X. Steirer, D.C. Olson, C. Ladam, D.S. Ginley, R.T. Collins, T.E. Furtak, Alkyl surface treatments of planar zinc oxide in hybrid organic/inorganic solar cells. *J. Phys. Chem. C* **116**, 8872 (2012)
37. S.J. Kim, J. Jung, D.H. Yoon, H.J. Kim, The effect of various solvents on the back channel of solution-processed In–Ga–Zn–O thin-film transistors intended for biosensor applications. *J. Phys. D. Appl. Phys.* **46**, 035102 (2013)
38. K. Lee, P.R. Nair, A. Scott, M.A. Alam, D.B. Janes, Device considerations for development of conductance-based biosensors. *J. Appl. Phys.* **105**, 102046 (2009)